Fast and Accurate Extrinsic Calibration for Multiple LiDARs and Cameras

Xiyuan Liu[1], Chongjian Yuan[1], and Fu Zhang[1]

***Abstract*—The combination of multiple sensors is becoming necessary in robotic applications as each sensor could complement the weakness of others. Determining a precise extrinsic parameter in a fast and reliable manner between multiple sensors is essential and remains challenging. In this paper, we propose a fast, accurate, and targetless extrinsic calibration method for multiple LiDARs and cameras based on adaptive voxelization. On the theory level, we incorporate the LiDAR extrinsic calibration with the bundle adjustment method. We derive the derivatives of the cost function w.r.t. the extrinsic parameter to accelerate the optimization. On the implementation level, we apply adaptive voxelization to reduce the computation time in the process of feature correspondence matching. The robustness and accuracy of our proposed method have been verified with experiments in outdoor test scenes under multiple LiDAR-camera configurations.**

***Index Terms*—Calibration, Sensor Fusion, Mapping.**

I. Introduction

MULTIPLE LiDARs and cameras have been increasingly used on mobile robots for missions such as autonomous navigation [1] and mapping [2]–[4]. This is due to the superior characteristics of the LiDAR in three-dimensional range detection and point cloud density, and the rich color information from the camera. The integration of multiple sensors could facilitate the state estimation of the robot [5] meanwhile producing a dense and colorized map (see Fig. 1). To better perceive the surrounding environment, it is worthwhile to transform the perceptions from multiple sensors into the same coordinate frame, i.e., to know the rigid transformation between each pair of sensors. In this paper, our work deals with the extrinsic calibration between multiple LiDARs and cameras.

Several challenges reside in the multi-sensor extrinsic calibration: (1) limited field-of-view (FoV) overlap among the sensors and the precision requirement. Current methods usually require the existence of common FoV between each pair of sensors [6]–[9], such that each feature is viewed by all sensors. In real-world applications, this FoV overlap might be minimal or not even exist due to numerous sensor mounting positions. The accuracy requirement of the calibration results, e.g., the consistency and colorization of the point cloud, is thus more challenging. (2) computation time demands. For general ICP-based LiDAR extrinsic calibration approaches [4, 10], the extrinsic is optimized by aligning the point cloud from all LiDARs and maximizing the point cloud's consistency. The increase in the number of LiDARs implies that the feature point correspondence searching will be more time-consuming. This is due to the reason that each feature point needs to search for and match with nearby feature points using a k-d tree which contains the whole point cloud. In the LiDAR-camera extrinsic calibration, a larger amount of LiDAR points will also lead to more computation time in the LiDAR feature extraction.

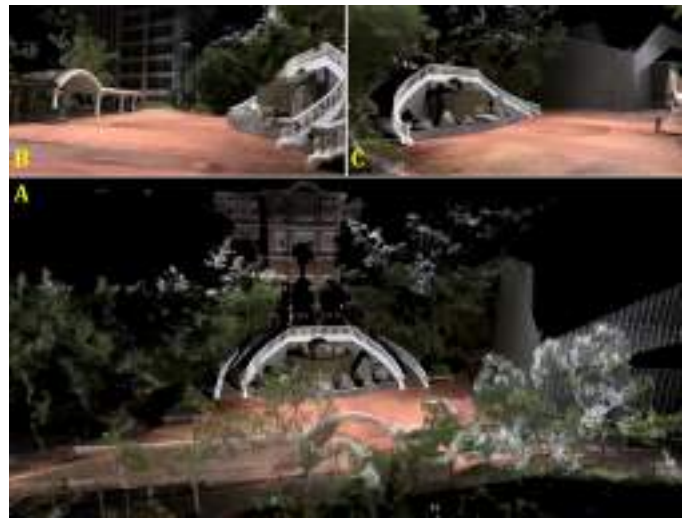

Fig. 1: A) The dense colorized point cloud with the LiDAR poses and extrinsic parameters optimized by our proposed method. The views from other perspectives are exhibited in B) left side and C) right side. Our experiment video is available at https://youtu.be/PaiYgAXl9iY.

To address the above challenges, we propose a fast and targetless approach for multiple LiDARs and cameras extrinsic calibration. To create co-visible features among all sensors, we introduce motions to the sensor platform such that each sensor will scan the same area (hence features) at different times. We first calibrate the extrinsic among LiDARs (and simultaneously estimate the LiDAR poses) by registering their point cloud using an efficient bundle adjustment (BA) method we recently proposed [3]. To reduce time consumption in feature correspondence matching among LiDARs, we implement an adaptive voxelization to dynamically segment the point cloud into multiple voxels that only one plane feature resides in each voxel. We then calibrate the extrinsic between the cameras and LiDARs by matching the co-visible features between the images and the above-reconstructed point cloud. To further accelerate the feature correspondence matching, we inherit the above adaptive voxel map to extract LiDAR edge features. In summary, our contributions are listed as follows:

[1]X. Liu, C. Yuan and F. Zhang are with the Department of Mechanical Engineering, The University of Hong Kong, Hong Kong Special Administrative Region, People's Republic of China. {xliuaa,ycj1}@connect.hku.hk, fuzhang@hku.hk

- We formulate the multi-LiDAR extrinsic calibration into a BA problem and implement an adaptive voxelization to accelerate the process of multi-LiDAR-camera extrinsic calibration. We boost the speed by more than 25 times for multi-LiDAR calibration and 1.5 times for multi-LiDAR-camera extrinsic calibration when compared to the state of the art [4, 11].
- We implement an automatic multi-LiDAR-camera extrinsic calibration pipeline. The precision and robustness of the proposed method have been validated in outdoor scenes with the average extrinsic translation and rotation errors down to 6mm and 0.09 degrees for LiDAR-camera, and 8mm and 0.2 degrees for LiDAR-LiDAR.
- We open source our implementation in ROS on GitHub[1] to benefit the robotics community.

II. Related Works

A. LiDAR-LiDAR Extrinsic Calibration

The extrinsic calibration methods between multiple LiDARs could be divided into motion-based and motionless approaches. Motion-based approaches assume each sensor undergoes the same rigid motion in each time interval [5, 12, 13] and transform the extrinsic calibration into a Hand-eye problem [14]. Authors in [15]–[17] also introduce external inertial navigation sensors to facilitate the motion estimation of LiDARs. The calibration precision of these approaches is easily affected by the accuracy of the LiDAR odometry results, which might be unreliable. Motionless methods have been discussed in [6, 7] where the authors attach retro-reflective tapes to the surface of calibration targets to create and facilitate the feature extraction among multiple LiDARs. These approaches require prior preparation work and FoV overlap between LiDARs, which is unpractical in real-world applications.

In our previous work [4], a simple rotational movement is introduced to eliminate the requirement of FoV overlap, as each onboard sensor could percept the same region of interest. Then the extrinsic parameter is calibrated, along with the estimation of LiDAR poses, by optimizing the consistency of the point cloud map with iterative closest point (ICP) registration. The main problem within [4] is that the ICP registration always registers one scan to the other, leading to an iterative process where only one optimization variable (e.g., extrinsic or LiDAR poses) can be optimized (by registering the point cloud affected by the variable under optimization to the rest). Such an iterative procedure is prolonged to converge. Moreover, at each iteration, the ICP-based feature correspondence matching process might be very time-consuming. As for each point-to-plane correspondence, ICP needs to either search inside a k-d tree containing the entire point cloud or create a k-d tree containing the local point cloud every time before searching.

In this work, we formulate the extrinsic calibration into a bundle adjustment (BA) problem [3], where all the optimization variables (both extrinsic and LiDAR poses) are optimized concurrently by registering points into their corresponding plane. When compared to other plane adjustment techniques [18, 19], the BA technique we use does not estimate the plane parameters in the optimization process but solves for them analytically in a closed-form solution prior to the optimization iteration. The removal of plane parameters from the optimization iteration lowers the dimension significantly and leads to very efficient multi-view registration. To match points corresponding to the same plane, we implement an adaptive voxelization technique [3] to replace the k-d tree in [4]. As only one plane feature exists in each voxel, our proposed work significantly saves the computation time in correspondence searching while remaining accurate (see Sec. III-B).

B. LiDAR-Camera Extrinsic Calibration

The extrinsic calibration between LiDAR and camera could be mainly divided into target-based and targetless methods. In target-based approaches, the geometric features, e.g., edges and surfaces, are extracted from artificial geometric solids [20]–[22] or chessboard [23, 24] using intensity and color information. These features are matched either automatically or manually and are solved with non-linear optimization tools. In [25], authors establish the constraints using the crosswalk features on the streets; however, this method is essentially target-based as the parallelism characteristic of the crosswalk is used. Since extra calibration targets and manual work are needed, these methods are less practical compared with targetless solutions.

The targetless methods could be further divided into motion-based and motionless approaches. In motion-based methods, the initial extrinsic parameter is usually estimated by the motion information and refined by the appearance information. In [26], authors reconstruct a point cloud from images using the structure from motion (SfM) to determine the initial extrinsic parameter and refine it by back-projecting LiDAR points onto the image plane. In [13, 27], authors initialize the extrinsic parameter by Hand-eye calibration and optimize it by minimizing the re-projection error between images and LiDAR scans. Though the introduction of motion addresses extra constraints between sensors, these methods require the sensor suite to move along a sufficiently excited trajectory. In motionless approaches, only the edge features that co-exist in both sensors' FoV are extracted and matched. Then the extrinsic parameter is optimized by minimizing the re-projected edge-to-edge distances [8, 11, 28, 29] or by maximizing the mutual information between the back-projected LiDAR points and the images [9].

Our proposed work is targetless and creates co-visible features by moving the sensor suite to multiple poses. Compared with [11] which extracts LiDAR edge features using RANSAC algorithm; our proposed work extracts edge features using the same adaptive voxelization already computed in the LiDAR extrinsic calibration, which is more competitive in computation time and calibration precision. Compared with [9] which uses LiDAR intensity information as a feature, our work uses more reliable 3D edge information and is more computationally efficient and accurate (see Sec. IV). Moreover, our work does not require the common FoV between sensors.

[1] https://github.com/hku-mars/mlcc

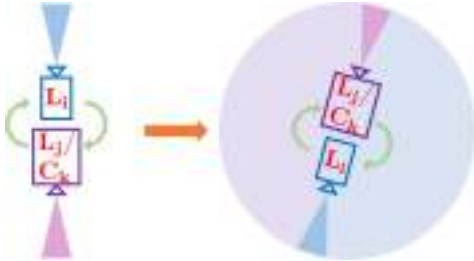

Fig. 2: FoV overlap created by rotation between two opposite pointing sensors. The original setup of two sensors L_i and L_j/C_k share no FoV overlap. With the introduction of rotational motion, the same region is scanned by all sensors across different times.

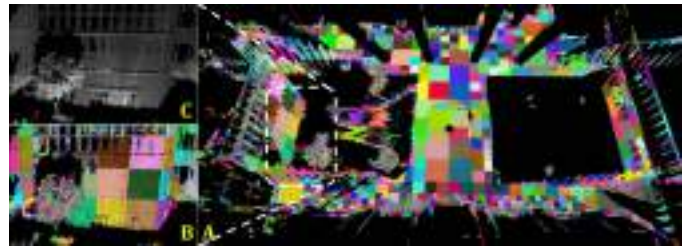

Fig. 3: A) LiDAR point cloud segmented with the adaptive voxelization. Points within the same voxel are colored identically. The detailed adaptive voxelization of points in the dashed white rectangle could be viewed in B) colored points and C) original points. The default size for the initial voxelization is 4m, and the minimum voxel size is 0.25m.

III. Methodology

A. Overview

Let ${}^B_A\mathbf{T} = ({}^B_A\mathbf{R}, {}^B_A\mathbf{t}) \in SE(3)$ represent the rigid transformation from frame A to frame B, where ${}^B_A\mathbf{R} \in SO(3)$ and ${}^B_A\mathbf{t} \in \mathbb{R}^3$ are the rotation and translation. We denote $\mathcal{L} = \{L_0, L_1, \cdots, L_{n-1}\}$ the set of n LiDARs, where L_0 represents the base LiDAR for reference, $\mathcal{C} = \{C_0, C_1, \cdots, C_h\}$ the set of h cameras, $\mathcal{E}_L = \{{}^{L_0}_{L_1}\mathbf{T}, {}^{L_0}_{L_2}\mathbf{T}, \cdots, {}^{L_0}_{L_{n-1}}\mathbf{T}\}$ the set of LiDAR extrinsic parameters and $\mathcal{E}_C = \{{}^{C_0}_{L_0}\mathbf{T}, {}^{C_1}_{L_0}\mathbf{T}, \cdots, {}^{C_h}_{L_0}\mathbf{T}\}$ the set of LiDAR-camera extrinsic parameters. To create co-visible features between multiple LiDARs and cameras that may share no FoV overlap, we rotate the robot platform to m poses such that the same region of interest is scanned by all sensors (see Fig. 2). Denote $\mathcal{T} = \{t_0, t_1, \cdots, t_{m-1}\}$ the time for each of the m poses and the pose of the base LiDAR at the initial time as the global frame, i.e., ${}^G_{L_0}\mathbf{T}_{t_0} = \mathbf{I}_{4\times4}$. Denote $\mathcal{S} = \{{}^G_{L_0}\mathbf{T}_{t_1}, {}^G_{L_0}\mathbf{T}_{t_2}, \cdots, {}^G_{L_0}\mathbf{T}_{t_{m-1}}\}$ the set of the base LiDAR poses in global frame. The point cloud patch scanned by LiDAR $L_i \in \mathcal{L}$ at time $t_j \in \mathcal{T}$ is denoted by $\mathcal{P}_{L_i,t_j}$, which is in L_i's local frame. This point cloud patch could be transformed to global frame by

$$\begin{aligned} {}^G\mathcal{P}_{L_i,t_j} &= {}^G_{L_i}\mathbf{T}_{t_j}\mathcal{P}_{L_i,t_j} \\ &\triangleq \{{}^G_{L_i}\mathbf{R}_{t_j}\mathbf{p}_{L_i,t_j} + {}^G_{L_i}\mathbf{t}_{t_j},\ \forall \mathbf{p}_{L_i,t_j} \in \mathcal{P}_{L_i,t_j}\}. \end{aligned} \tag{1}$$

In our proposed approach of multi-sensor calibration, we sequentially calibrate the $\mathcal{E}_L$ and $\mathcal{E}_C$. In the first step, we simultaneously estimate the LiDAR extrinsic $\mathcal{E}_L$ and the base lidar pose trajectory $\mathcal{S}$ based on an efficient multi-view registration (see Sec. III-C). In the second step, we calibrate the $\mathcal{E}_C$ by matching the depth-continuous edges extracted from images and the above-reconstructed point cloud (see Sec. III-D). Lying in the center of both LiDAR and camera extrinsic calibration is an adaptive map, which finds correspondence among LiDAR and camera measurements efficiently (Sec. III-B).

B. Adaptive Voxelization

To find the correspondences among different LiDAR scans, we assume the initial base LiDAR trajectory $\mathcal{S}$, LiDAR extrinsic $\mathcal{E}_L$, and camera extrinsic $\mathcal{E}_C$ are available. The initial base LiDAR trajectory $\mathcal{S}$ could be obtained by an online LiDAR SLAM (e.g., [2]), and the initial extrinsic could be obtained from the CAD design or a rough Hand-eye calibration [14]. Our previous work [4] extracts edge and plane feature points from each LiDAR scan and matches them to the nearby edge and plane points in the map by a k-nearest neighbor search (kNN). This would repeatedly build a k-d tree of the global map at each iteration. In this paper, we use a more efficient voxel map proposed in [3] to create correspondences among all LiDAR scans.

The voxel map is built by cutting the point cloud (registered using the current $\mathcal{S}$ and $\mathcal{E}_L$) into small voxels such that all points in a voxel roughly lie on a plane (with some adjustable tolerance). The main problem of the fixed-resolution voxel map is that if the resolution is high, the segmentation would be too time-consuming, while if the resolution is too low, multiple small planes in the environments falling into the same voxel would not be segmented. To best adapt to the environment, we implement an adaptive voxelization process. More specifically, the entire map is first cut into voxels with a pre-set size (usually large, e.g., 4m). Then for each voxel, if the contained points from all LiDAR scans roughly form a plane (by checking the ratio between eigenvalues), it is treated as a planar voxel; otherwise, they will be divided into eight octants, where each will be examined again until the contained points roughly form a plane or the voxel size reaches the pre-set minimum lower bound. Moreover, the adaptive voxelization is performed directly on the LiDAR raw points, so no prior feature points extraction is needed as in [4].

Fig. 3 shows a typical result of the adaptive voxelization process in a complicated campus environment. As can be seen, this process is able to segment planes of different sizes, including large planes on the ground, medium planes on the building walls, and tiny planes on tree crowns.

C. Multi-LiDAR Extrinsic Calibration

With adaptive voxelization, we can obtain a set of voxels of different sizes. Each voxel contains points that are roughly on a plane and creates a planar constraint for all LiDAR poses that have points in this voxel. More specifically, considering the l-th voxel consisting of a group of points $\mathcal{P}_l = \{{}^G\mathbf{p}_{L_i,t_j}\}$ scanned by $L_i \in \mathcal{L}$ at times $t_j \in \mathcal{T}$. We define a point cloud consistency indicator $c_l\left({}^G_{L_i}\mathbf{T}_{t_j}\right)$ which forms a factor on $\mathcal{S}$ and $\mathcal{E}_L$ as shown in Fig. 4(a). Then, the base LiDAR trajectory and extrinsic are estimated by optimizing the factor graph. A

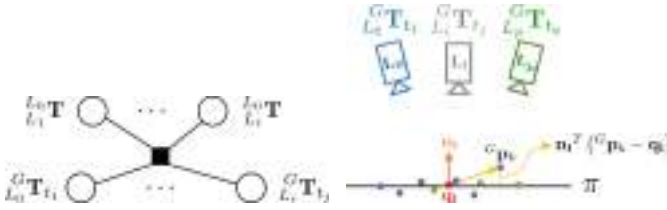

(a) (b)

Fig. 4: (a) The l-th factor item relating to $\mathcal{S}$ and $\mathcal{E}_L$ with $L_i \in \mathcal{L}$ and $t_j \in \mathcal{T}$. (b) The distance from the point ${}^G\mathbf{p}_k$ to the plane $\boldsymbol{\pi}$.

natural choice for the consistency indicator $c_l(\cdot)$ would be the summed Euclidean distance between each ${}^G\mathbf{p}_{L_i,t_j}$ to the plane to be estimated (see Fig. 4(b)). Taking account of all such indicators within the voxel map, we could formulate the problem as

$$\arg\min_{\mathcal{S},\mathcal{E}_L,\mathbf{n}_l,\mathbf{q}_l} \sum_l \underbrace{\left(\frac{1}{N_l} \sum_{k=1}^{N_l} \left(\mathbf{n}_l^T \left({}^G\mathbf{p}_k - \mathbf{q}_l \right) \right)^2 \right)}_{l\text{-th factor}}, \tag{2}$$

where ${}^G\mathbf{p}_k \in \mathcal{P}_l$, N_l is the total number of points in $\mathcal{P}_l$, $\mathbf{n}_l$ is the normal vector of the plane and $\mathbf{q}_l$ is a point on this plane. The optimization dimension in (2) is too high due to the dependence on the planar parameters $\boldsymbol{\pi} = (\mathbf{n}_l, \mathbf{q}_l)$. Fortunately, since one plane parameter is independent from another, we can optimize over $(\mathbf{n}_l, \mathbf{q}_l)$ first, i.e.,

$$\arg\min_{\mathcal{S},\mathcal{E}_L} \sum_l \left(\min_{\mathbf{n}_l,\mathbf{q}_l} \frac{1}{N_l} \sum_{k=1}^{N_l} \left(\mathbf{n}_l^T \left({}^G\mathbf{p}_k - \mathbf{q}_l \right) \right)^2 \right). \tag{3}$$

The inner optimization over $(\mathbf{n}_l, \mathbf{q}_l)$ in (3) could be further performed on $\mathbf{q}_l$ first and on $\mathbf{n}_l$ then, i.e.,

$$\arg\min_{\mathbf{n}_l} \left(\min_{\mathbf{q}_l} \frac{1}{N_l} \sum_{k=1}^{N_l} \left(\mathbf{n}_l^T \left({}^G\mathbf{p}_k - \mathbf{q}_l \right) \right)^2 \right). \tag{4}$$

As can be seen, the cost function in (4) is quadratic w.r.t. $\mathbf{q}_l$. Hence the inner optimization can be solved analytically by setting the derivatives to zeros, i.e.,

$$\mathbf{n}_l \mathbf{n}_l^T \left(\frac{1}{N_l} \sum_{k=1}^{N_l} \left({}^G\mathbf{p}_k - \mathbf{q}_l \right) \right) = \mathbf{0}. \tag{5}$$

It is seen that the solution to (5) is not unique as long as $\sum_{k=1}^{N_l} \left({}^G\mathbf{p}_k - \mathbf{q}_l \right)$ is perpendicular to $\mathbf{n}_l$, which allows $\mathbf{q}_l$ to move freely along any direction perpendicular to $\mathbf{n}_l$. Since this free movement of $\mathbf{q}_l$ does not change the plane parameterized by it, nor affect the cost function in (4), any solution of $\mathbf{q}_l$ satisfying (5) would be an optimal solution to the inner optimization problem of (4). One such solution could be

$$\mathbf{q}_l^* = \frac{1}{N_l} \sum_{k=1}^{N_l} {}^G\mathbf{p}_k. \tag{6}$$

Substituting the optimal solution of $\mathbf{q}_l$ in (6) back to (4) leads to

$$\arg\min_{\|\mathbf{n}_l\|=1} \mathbf{n}_l^T \underbrace{\left(\frac{1}{N_l} \sum_{k=1}^{N_l} {}^G\mathbf{p}_k \, {}^G\mathbf{p}_k^T - \mathbf{q}_l^* \mathbf{q}_l^{*T} \right)}_{\mathbf{A}_l} \mathbf{n}_l. \tag{7}$$

Again, this optimization problem has the well-known analytical optimal solution $\mathbf{n}_l^*$, which is the eigenvector corresponding to the smallest eigenvalue λ_3 of the matrix $\mathbf{A}_l$. As a result, substituting the optimal $\mathbf{n}_l^*$ back to (3) leads to

$$\mathcal{S}^*, \mathcal{E}_L^* = \arg\min_{\mathcal{S},\mathcal{E}_L} \sum_l \lambda_3 \left(\mathbf{A}_l \right). \tag{8}$$

As can be seen, the optimization variables $(\mathbf{n}_l, \mathbf{q}_l)$ are analytically solved before the optimization, which significantly reduces the optimization dimension. The resultant optimization in (8) is over the LiDAR pose ${}^G_{L_i}\mathbf{T}_{t_j}$ (hence the base LiDAR trajectory $\mathcal{S}$ and extrinsic $\mathcal{E}_L$) only. To see this, we note that $\mathbf{A}_l$ depends on ${}^G\mathbf{p}_k$ (directly or via $\mathbf{q}_l^*$ in (6)), which is observed locally by pose ${}^G_{L_i}\mathbf{T}_{t_j}$.

The optimization in (8) is nonlinear and solved iteratively. In each iteration, the cost function is approximated to the second order. More specifically, we view λ_3 as a function of all the contained points ${}^G\mathbf{p}$ which is the column vector containing each ${}^G\mathbf{p}_k \in \mathcal{P}_l$:

$${}^G\mathbf{p} = [{}^G\mathbf{p}_1^T \, {}^G\mathbf{p}_2^T \cdots {}^G\mathbf{p}_{N_l}^T]^T \in \mathbb{R}^{3N_l}.$$

The $\lambda_3({}^G\mathbf{p})$ in (8) could be approximated by

$$\lambda_3 \left({}^G\mathbf{p} + \delta {}^G\mathbf{p} \right) \approx \lambda_3 \left({}^G\mathbf{p} \right) + \mathbf{J} \cdot \delta {}^G\mathbf{p} + \frac{1}{2} \delta {}^G\mathbf{p}^T \cdot \mathbf{H} \cdot \delta {}^G\mathbf{p}, \tag{9}$$

where $\mathbf{J}$ and $\mathbf{H}$ are the first and second derivatives of $\lambda_3({}^G\mathbf{p})$ w.r.t. ${}^G\mathbf{p}$. The detailed derivation of $\mathbf{J}$ and $\mathbf{H}$ could be found in [3] and is omitted here due to space limit.

Suppose the k-th point ${}^G\mathbf{p}_k$ in ${}^G\mathbf{p}$ is scanned by LiDAR L_i at time t_j, then

$$\begin{aligned} {}^G\mathbf{p}_k &= {}^G_{L_i}\mathbf{T}_{t_j} \mathbf{p}_k = {}^G_{L_0}\mathbf{T}_{t_j} \cdot {}^{L_0}_{L_i}\mathbf{T} \cdot \mathbf{p}_k \\ &= {}^G_{L_0}\mathbf{R}_{t_j} \left({}^{L_0}_{L_i}\mathbf{R} \cdot \mathbf{p}_k + {}^{L_0}_{L_i}\mathbf{t} \right) + {}^G_{L_0}\mathbf{t}_{t_j}, \end{aligned} \tag{10}$$

which implies ${}^G\mathbf{p}_k$ is dependent on $\mathcal{S}$ and $\mathcal{E}_L$. To perturb ${}^G\mathbf{p}_k$, we perturb a pose $\mathbf{T}$ in its tangent plane $\delta\mathbf{T} = [\boldsymbol{\phi}^T \ \delta\mathbf{t}^T]^T \in \mathbb{R}^6$ with the $\boxplus$ as defined in [30], i.e.,

$$\begin{aligned} \mathbf{T} &= (\mathbf{R}, \mathbf{t}) \\ \mathbf{T} \boxplus \delta\mathbf{T} &= \left(\mathbf{R} \exp\left(\boldsymbol{\phi}^\wedge \right), \mathbf{t} + \delta\mathbf{t} \right). \end{aligned} \tag{11}$$

Based on the error parameterization in (11) for both ${}^G_{L_0}\mathbf{T}_{t_j}$ and extrinsic ${}^{L_0}_{L_i}\mathbf{T}$, the perturbed point location in (10) is

$$\begin{aligned} {}^G\mathbf{p}_k + \delta {}^G\mathbf{p}_k = {}^G_{L_0}\mathbf{R}_{t_j} \exp\left({}^G_{L_0}\boldsymbol{\phi}^\wedge_{t_j} \right) \Big({}^{L_0}_{L_i}\mathbf{R} \exp\left({}^{L_0}_{L_i}\boldsymbol{\phi}^\wedge \right) \mathbf{p}_k \\ + {}^{L_0}_{L_i}\mathbf{t} + \delta {}^{L_0}_{L_i}\mathbf{t} \Big) + {}^G_{L_0}\mathbf{t}_{t_j} + \delta {}^G_{L_0}\mathbf{t}_{t_j}. \end{aligned} \tag{12}$$

Then, subtracting (10) from (12), we obtain

$$\begin{aligned} \delta {}^G\mathbf{p}_k \approx {}^G_{L_0}\mathbf{R}_{t_j} \left({}^{L_0}_{L_i}\mathbf{R}\mathbf{p}_k + {}^{L_0}_{L_i}\mathbf{t} \right)^\wedge {}^G_{L_0}\boldsymbol{\phi}_{t_j} + \delta {}^G_{L_0}\mathbf{t}_{t_j} + \\ {}^G_{L_i}\mathbf{R}_{t_j} \left(\mathbf{p}_k \right)^\wedge {}^{L_0}_{L_i}\boldsymbol{\phi} + {}^G_{L_0}\mathbf{R}_{t_j} \delta {}^{L_0}_{L_i}\mathbf{t} \end{aligned} \tag{13}$$

and

$$\delta^G\mathbf{p} = \mathbf{D}\cdot\delta\mathbf{x}, \tag{14}$$

where

$$\delta\mathbf{x} = [\cdots \ {}^{G}_{L_0}\boldsymbol{\phi}_{t_j}^T \ \delta{}^{G}_{L_0}\mathbf{t}_{t_j}^T \cdots {}^{L_0}_{L_i}\boldsymbol{\phi}^T \ \delta{}^{L_0}_{L_i}\mathbf{t}^T \cdots]^T \in \mathbb{R}^{6(m+n-2)}$$

is a small perturbation of the entire optimization vector $\mathbf{x}$

$$\mathbf{x} = [\cdots \ {}^{G}_{L_0}\mathbf{R}_{t_j} \ \ {}^{G}_{L_0}\mathbf{t}_{t_j} \cdots {}^{L_0}_{L_i}\mathbf{R} \ \ {}^{L_0}_{L_i}\mathbf{t} \cdots],$$

and

$$\mathbf{D} = \begin{bmatrix} \vdots & \vdots \\ \cdots \ \mathbf{D}^{\mathcal{S}}_{k,p} \ \cdots & \mathbf{D}^{\mathcal{E}_L}_{k,q} \ \cdots \\ \vdots & \vdots \end{bmatrix} \in \mathbb{R}^{3N_l\times 6(m+n-2)}$$

$$\mathbf{D}^{\mathcal{S}}_{k,p} = \begin{cases} \left[-{}^{G}_{L_0}\mathbf{R}_{t_j}\left({}^{L_0}_{L_i}\mathbf{R}\mathbf{p}_k + {}^{L_0}_{L_i}\mathbf{t}\right)^{\wedge} \ \mathbf{I}\right], & \text{if } p = j \\ \mathbf{0}_{3\times 6}, & \text{else} \end{cases}$$

$$\mathbf{D}^{\mathcal{E}_L}_{k,q} = \begin{cases} \left[-{}^{G}_{L_0}\mathbf{R}_{t_j} \ {}^{L_0}_{L_i}\mathbf{R}\left(\mathbf{p}_k\right)^{\wedge} \ \ {}^{G}_{L_0}\mathbf{R}_{t_j}\right], & \text{if } q = i \\ \mathbf{0}_{3\times 6}, & \text{else.} \end{cases} \tag{15}$$

Substituting (14) to (9) leads to

$$\begin{aligned} \lambda_3(\mathbf{x}\boxplus\delta\mathbf{x}) &\approx \lambda_3(\mathbf{x}) + \mathbf{J}\mathbf{D}\delta\mathbf{x} + \frac{1}{2}\delta\mathbf{x}^T\mathbf{D}^T\mathbf{H}\mathbf{D}\delta\mathbf{x} \\ &= \lambda_3(\mathbf{x}) + \bar{\mathbf{J}}\delta\mathbf{x} + \frac{1}{2}\delta\mathbf{x}^T\bar{\mathbf{H}}\delta\mathbf{x}. \end{aligned} \tag{16}$$

Then the optimal $\mathbf{x}^*$ could be determined by iteratively solving the (17) with the LM method and updating the $\delta\mathbf{x}$ to $\mathbf{x}$.

$$\left(\bar{\mathbf{H}} + \mu\mathbf{I}\right)\delta\mathbf{x} = -\bar{\mathbf{J}}^T \tag{17}$$

D. LiDAR-Camera Extrinsic Calibration

With the LiDAR extrinsic parameter $\mathcal{E}_L$ and pose trajectory $\mathcal{S}$ computed above, we obtain a dense global point cloud by transforming all LiDAR points to the base LiDAR frame. Then, the extrinsic $\mathcal{E}_C$ is optimized by minimizing the summed distance between the back-projected LiDAR edge feature points and the image edge feature points. Two types of LiDAR edge points could be extracted from the point cloud. One is the depth-discontinuous edges between the foreground and background objects, and the other is the depth-continuous edge between two neighboring non-parallel planes. As explained in [11], depth-discontinuous edges suffer from foreground inflation and bleeding points phenomenon; we hence use depth-continuous edges to match point cloud and images.

In [11], the LiDAR point cloud is segmented into voxels with uniform size, and the planes inside each voxel are estimated by the RANSAC algorithm. In contrast, our method uses the same adaptive voxel map obtained in Sec. III-B. We calculate the angle between their containing plane normals for every two adjacent voxels. If this angle exceeds a threshold, the intersection line of these two planes is extracted as the depth-continuous edge, as shown in Fig. 5. We choose to implement the Canny algorithm for image edge features to detect and extract.

Suppose ${}^G\mathbf{p}_i$ represents the i-th point from a LiDAR edge feature extracted above in global frame. With pin-hole camera

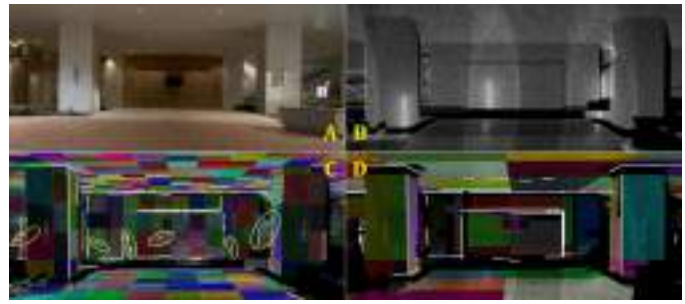

Fig. 5: Depth-continuous LiDAR edge feature extraction comparison. A) Real-world image. B) Raw point cloud of this scene. C) Edges extracted using method in [11] where the yellow circles indicate the false estimations. D) Edges extracted with adaptive voxelization.

and its distortion model, ${}^G\mathbf{p}_i$ is projected onto the image taken by camera C_l at t_j, i.e., $\mathbf{I}_{l,j}$ by

$${}^{\mathbf{I}_{l,j}}\mathbf{p}_i = \mathbf{f}\left(\boldsymbol{\pi}\left({}^{C_l}_{L_0}\mathbf{T}\left({}^{G}_{L_0}\mathbf{T}_{t_j}\right)^{-1}{}^G\mathbf{p}_i\right)\right), \tag{18}$$

where $\mathbf{f}(\cdot)$ is the camera distortion model and $\boldsymbol{\pi}(\cdot)$ is the projection model. Let $\mathcal{I}_i$ represent the set of images that capture the point ${}^G\mathbf{p}_i$, i.e., $\mathcal{I}_i = \{\mathbf{I}_{l,j}\}$. For each ${}^{\mathbf{I}_{l,j}}\mathbf{p}_i$, the κ nearest image edge feature points $\mathbf{q}_k$ on $\mathbf{I}_{l,j}$ are searched. The normal vector $\mathbf{n}_{i,l,j}$ of the edge formed by these κ points is thus the eigenvector corresponding to the minimum eigenvalue of $\mathbf{A}_{i,l,j}$ that

$$\mathbf{A}_{i,l,j} = \sum_{k=1}^{\kappa}(\mathbf{q}_k - \mathbf{q}_{i,l,j})(\mathbf{q}_k - \mathbf{q}_{i,l,j})^T, \mathbf{q}_{i,l,j} = \frac{1}{\kappa}\sum_{k=1}^{\kappa}\mathbf{q}_k. \tag{19}$$

The residual originated from this LiDAR camera correspondence is defined as

$$\mathbf{r}_{i,l,j} = \mathbf{n}_{i,l,j}^T\left({}^{\mathbf{I}_{l,j}}\mathbf{p}_i - \mathbf{q}_{i,l,j}\right). \tag{20}$$

Collecting all such correspondences, the extrinsic $\mathcal{E}_C$ calibration problem could be formulated as

$$\mathcal{E}_C^* = \arg\min_{\mathcal{E}_C}\sum_i\sum_{\mathbf{I}_{l,j}\in\mathcal{I}_i}\left(\mathbf{n}_{i,l,j}^T\left({}^{\mathbf{I}_{l,j}}\mathbf{p}_i - \mathbf{q}_{i,l,j}\right)\right). \tag{21}$$

Inspecting the residual in (20), we find the ${}^{\mathbf{I}_{l,j}}\mathbf{p}_i$ is dependent on LiDAR poses ${}^{G}_{L_0}\mathbf{T}_{t_j}$. This is due to the reason that LiDARs may have FoV overlap with cameras at different times (as in Fig. 2). Since ${}^{G}_{L_0}\mathbf{T}_{t_j} \in \mathcal{S}$ has been well estimated from Sec. III-C, we keep them fixed in this step. Moreover, the $\mathbf{n}_{i,l,j}$ and $\mathbf{q}_{i,l,j}$ are also implicitly dependent on $\mathcal{E}_C$, since both $\mathbf{n}_{i,l,j}$ and $\mathbf{q}_{i,l,j}$ are related with nearest neighbor search. The complete derivative of (21) to the variable $\mathcal{E}_C$ would be too complicated. In this paper, to simplify the optimization problem, we ignore the influence of camera extrinsic on $\mathbf{n}_{i,l,j}$ and $\mathbf{q}_{i,l,j}$. This strategy works well in practice as detailed in Sec. IV-C.

The non-linear optimization (21) is solved with LM method by approximating the residuals with their first order derivatives (22). The optimal $\mathcal{E}_C^*$ is then obtained by iteratively solving (22) and updating $\delta\mathbf{x}$ to $\mathbf{x}$ using the $\boxplus$ operation as (11).

$$\delta\mathbf{x} = -\left(\mathbf{J}^T\mathbf{J} + \mu\mathbf{I}\right)^{-1}\mathbf{J}^T\mathbf{r}, \tag{22}$$

where

$$\delta\mathbf{x} = \begin{bmatrix} \cdots & {}^{C_l}_{L_0}\boldsymbol{\phi}^T & {}^{C_l}_{L_0}\delta\mathbf{t}^T & \cdots \end{bmatrix}^T \in \mathbb{R}^{6h}$$
$$\mathbf{x} = \begin{bmatrix} \cdots & {}^{C_l}_{L_0}\mathbf{R} & {}^{C_l}_{L_0}\mathbf{t} & \cdots \end{bmatrix}$$
$$\mathbf{J} = \begin{bmatrix} \cdots & \mathbf{J}_p^T & \cdots \end{bmatrix}^T, \mathbf{r} = \begin{bmatrix} \cdots & \mathbf{r}_p & \cdots \end{bmatrix}^T,$$

with $\mathbf{J}_p$ and $\mathbf{r}_p$ being the sum of $\mathbf{J}_{i,l,j}$ and $\mathbf{r}_{i,l,j}$ when $l = p$:

$$\mathbf{J}_{i,l,j} = \mathbf{n}_{i,l,j}^T \frac{\partial \mathbf{f}(\mathbf{p})}{\partial \mathbf{p}} \frac{\partial \boldsymbol{\pi}(\mathbf{P})}{\partial \mathbf{P}} \begin{bmatrix} -{}^{C_l}_{L_0}\mathbf{R}\left({}^{L_0}\mathbf{p}_i\right)^\wedge & \mathbf{I} \end{bmatrix} \in \mathbb{R}^{1\times 6}$$
$${}^{L_0}\mathbf{p}_i = \left({}^{G}_{L_0}\mathbf{T}_{t_j}\right)^{-1} {}^{G}\mathbf{p}_i. \tag{23}$$

E. Calibration Pipeline

The workflow of our proposed multi-sensor calibration is illustrated in Fig. 6. At the beginning of the calibration, the base LiDAR's raw point cloud is processed by a LOAM algorithm [2] to obtain the initial base LiDAR trajectory $\mathcal{S}$. Then, the raw point cloud of all LiDARs are segmented by time into point cloud patches, i.e., $\mathcal{P}_{L_i,t_j}, L_i \in \mathcal{L}, t_j \in \mathcal{T}$ that is collected under the pose ${}^{G}_{L_i}\mathbf{T}_{t_j}$.

In multi-LiDAR extrinsic calibration, the base LiDAR poses $\mathcal{S}$ are first optimized using the base LiDAR's point cloud patches $\mathcal{P}_{L_0,t_j}$. It is noticed that only $\mathcal{S}$ is involved and optimized in (3). Then the extrinsic $\mathcal{E}_L$ are calibrated by aligning the point cloud from the LiDAR to be calibrated with those from the base LiDAR. In this stage's problem formulation (3), $\mathcal{S}$ is fixed at the optimized values from the previous stage, and only $\mathcal{E}_L$ is optimized. Finally, both $\mathcal{S}$ and $\mathcal{E}_L$ are jointly optimized using the entire point cloud patches. In each iteration of the optimization (over $\mathcal{S}$, $\mathcal{E}_L$, or both), the adaptive voxelization (as described in Sec. III-B) is performed with the current value of $\mathcal{S}$ and $\mathcal{E}_L$. Moreover, as implied by (9), the Hessian matrix $\mathbf{H}$ has a computation complexity of $O(N^2)$, where N is the number of points. In practice, to reduce this computational complexity, we down-sample the number of points scanned from the same LiDAR to 4 in each voxel. Such a process would lower the time complexity of the proposed algorithm to $O(N_{voxel})$, where N_{voxel} is the total number of adaptive voxels. In Sec. IV-B2, $N_{voxel} \approx 9 \times 10^3$ which is greatly smaller than the total number of raw LiDAR points in this scene, i.e., $N_{points} \approx 4 \times 10^7$.

In multi-LiDAR-camera extrinsic calibration, the adaptive voxel map obtained with the $\mathcal{S}^*$ and $\mathcal{E}_L^*$ in the previous step is used to extract the depth-continuous edges (Sec. III-D). Then those three-dimension edges are back-projected onto each image using the extrinsic parameter $\mathcal{E}_C$ and are matched with two-dimension Canny edges extracted from the image. By minimizing the residuals defined by these two edges, we iteratively solve for the optimal $\mathcal{E}_C^*$ with the Ceres Solver[2].

IV. Experiments and Results

To test the proposed algorithm, we customized a remotely operated vehicle platform[3] (see Fig. 7) with one Livox AVIA LiDAR[4] (with 70.4 degrees of FoV, see L_3 in Fig. 7), one Livox MID-100 LiDAR[5] (which has three internal MID-40 LiDARs, each has 38.4 degrees of FoV, see L_0, L_1, and L_2 in Fig. 7) and two MV-CA013-21UC[6] cameras (with 82.9 degrees of FoV each, see C_1 and C_2 in Fig. 7). The extrinsic parameters of the three MID-40 inside the MID-100 have been calibrated by the manufacturer and could be used as the ground truth for the calibration evaluation. Note that the two types of LiDAR units (e.g., AIVIA and MID-40) have different scanning patterns, densities, and FoVs.

We have verified our proposed algorithm with the data collected in two random test scenes in our campus, as shown in Fig. 8. Scene-1 is a square in front of the library with moving pedestrians, and scene-2 is an area near a garden. In Sec. IV-A, the data collected in our previous work [4] have also been used

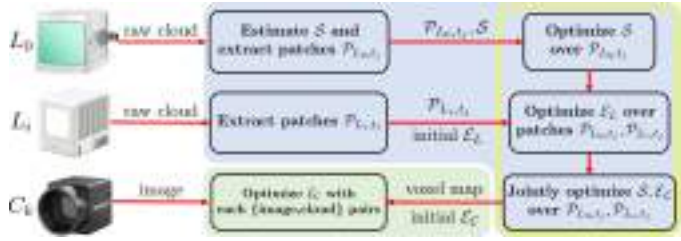

Fig. 6: The workflow of our proposed method: multi-LiDAR extrinsic calibration (light blue region) and LiDAR-camera extrinsic calibration (light green region). The adaptive voxelization takes effect in the steps surrounded by the yellow rectangle.

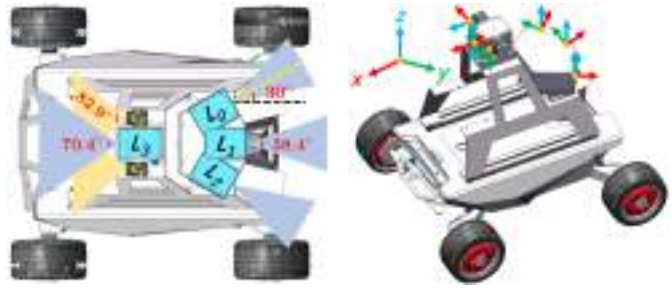

(a) (b)

Fig. 7: Our customized multi-sensor vehicle platform. Left: the FoV coverage of each sensor with their FoV specs. Right: the orientation of each sensor is denoted in the right-handed coordinate system.

(a) Scene-1 (b) Scene-2

Fig. 8: Our experiment test scenes.

[2]http://ceres-solver.org/

[3]https://www.agilex.ai/product/3?lang=en-us

[4]https://www.livoxtech.com/avia

[5]https://www.livoxtech.com/mid-40-and-mid-100

[6]https://www.rmaelectronics.com/hikrobot-mv-ca013-21uc/

for comparison with the previous method. All experiments are conducted on a desktop computer with an i7-9700K processor and 32GB RAM.

For our proposed multi-LiDAR extrinsic calibration, we first conduct a standard Hand-eye calibration [14] with an '8'-figure path to initialize the extrinsic $\mathcal{E}_L$. Then we rotate our multi-sensor platform slightly more than 360 degrees and keep the robot platform still every few degrees, such that we can acquire dense enough point cloud from each LiDAR at each pose. Keeping the robot platform still during data collection also eliminates the problem caused by motion distortion and time synchronization. The timestamps $\mathcal{T}$ are manually selected that only the point cloud and image data are selected when the robot platform is still.

A. Convergence and Computation Time Comparison

In this section, we demonstrate that the proposed algorithm converges much faster than our previous work [4] in terms of both iteration times and computation time while remaining accurate. We use the dataset collected in [4] on MID-100 and choose the middle MID-40 as the base LiDAR to calibrate the adjacent two LiDARs. We perform 10 independent trials that in each trial the initial extrinsic $\mathcal{E}_L$ is randomly perturbed (± 10 degrees for ${}^{L_1}_{L_i}\mathbf{R}$ and ± 0.2m for ${}^{L_1}_{L_i}\mathbf{t}$) from the manufacturer's calibrated values.

The extrinsic rotation and translation errors of both methods versus iteration time are plotted in Fig. 9 and the averaged time cost per iteration in each step of both methods is summarized in Table I. It is shown in Fig. 9 that the proposed work makes both the extrinsic translation and rotation errors quickly converge to the appropriate values. This is due to the second-order optimization we used in Sec. III-C, where the Jacobian and Hessian matrix with respect to the optimization variables ($\mathcal{S}$ and $\mathcal{E}_L$) are exactly derived. In contrast, in the previous work [4], only the Jacobian of the residual w.r.t. one LiDAR is considered, causing inaccurate Jacobian computation. The implementation of adaptive voxelization also significantly reduces the time cost in feature correspondence matching compared with k-d tree search in [4]. The calibration results of both methods in the above 10 trials are plotted in Fig. 10 which indicates that the increase in speed of our proposed method does not result in the loss of accuracy. Considering the speed-raising in computation time (more than 5 times faster) and the convergence rate (5 times faster), our proposed algorithm could considerably shorten the total calibration time.

TABLE I: COMPUTATION TIME PER ITERATION

	Pose Optimize	Extrinsic Optimize	Global Optimize
Previous Work [4]	6.7715s	5.7367s	15.1252s
Proposed	**0.3827s**	**0.5365s**	**3.4598s**

To quantify the convergence basin of our proposed method, we further apply multiple setups of external noises to $\mathcal{E}_L$ as the initial seed. In each configuration, the initial extrinsic is randomly perturbed (± 10 degrees for rotation and ± 0.5m for translation) from the manufacturer's calibrated values. As

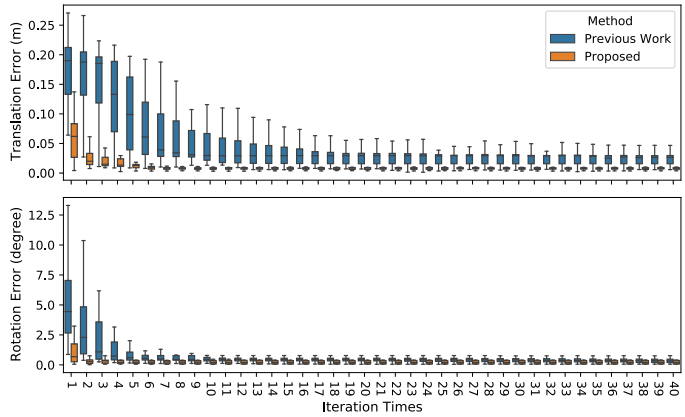

Fig. 9: Convergence comparison of the proposed method and our previous work [4]. Each box-plot consists of 40 values from 10 trials, two test scenes and two LiDAR pairs, i.e., $\{L_1, L_0\}, \{L_1, L_2\}$. The mean and standard deviation of the initial extrinsic errors are 0.1752m and 0.0489m for translation and 7.9819 degrees and 3.0541 degrees for rotation, respectively.

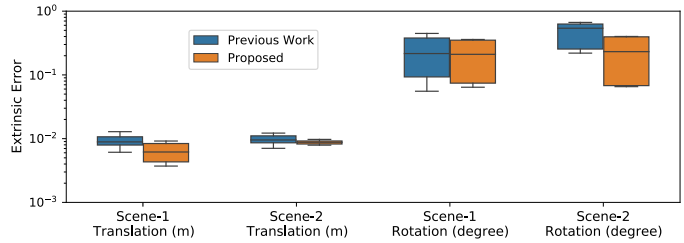

Fig. 10: Extrinsic calibration results of three MID-40 LiDARs. Each box-plot consists of 20 values respectively from 10 trials and two pairs of LiDARs.

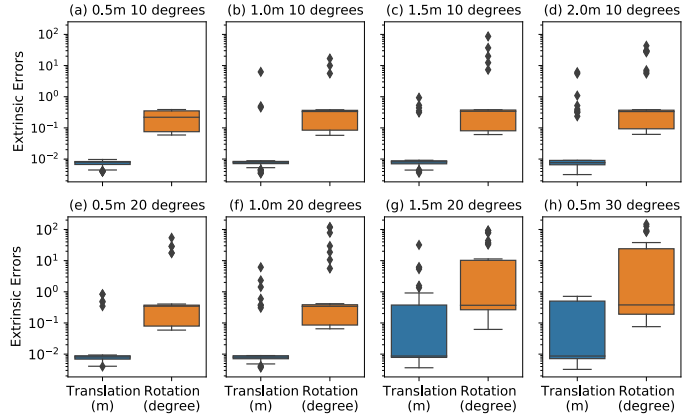

Fig. 11: The distribution of calibration errors under disturbed initial values. Each box-plot consists of 40 values respectively from 10 trials, two test scenes and two pairs of LiDARs.

illustrated in Fig. 11, given the rotation noise level of 10 degrees, the proposed method could ideally converge when the level of translation noise is 0.5m and mostly converge when the translation noise is under 1.5m. When the rotation noise is 20 degrees, our proposed method could generally converge when the translation noise is under 1.0m. We believe this noise level could sufficiently cover the scenarios in the real-world caused by manufacturing or mounting errors.

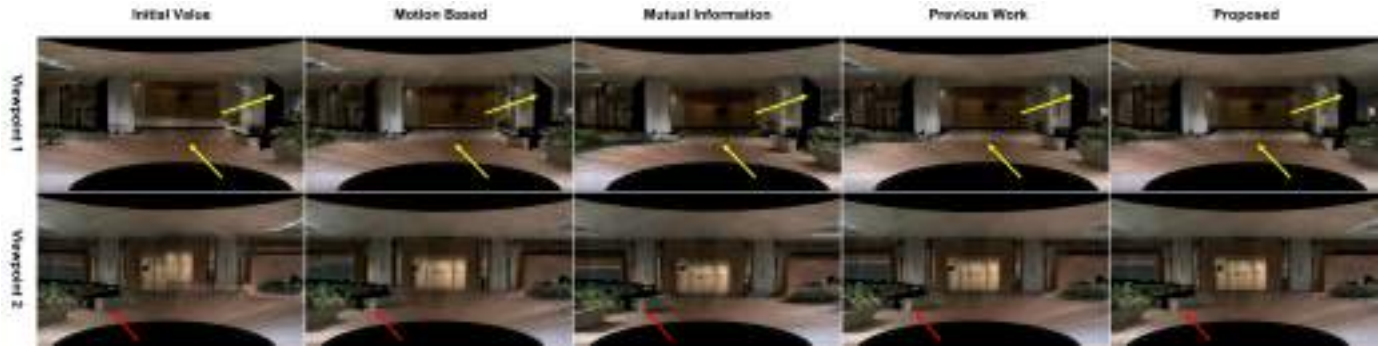

Fig. 12: Point cloud colorized using extrinsic calibrated by [9, 11, 13] and our proposed method. Each row represents a viewpoint in scene-2. The detailed difference between these methods are pointed out by arrows, e.g., miss-colorization on pillars and benches (zoomed view is recommended).

B. Multi-LiDAR Calibration

1) MID-100 LiDAR Self Calibration: In this section, we compare our algorithm with the motion-based method [13] using the MID-100 LiDAR (see Fig. 7) and the data collected in both test scenes. The middle MID-40 is chosen as the base LiDAR to calibrate the extrinsic $\mathcal{E}_L$ of other MID-40s, i.e., ${}^{L_1}_{L_0}\mathbf{T}, {}^{L_1}_{L_2}\mathbf{T}$. For both methods, the extrinsic $\mathcal{E}_L$ are initialized by the Hand-eye calibration, and the results are summarized in Table II. Since the MID-40 LiDAR is of small FoV and the vehicle's movements in both test scenes are limited to planar motions, the motion-based method is less comparable to our proposed method.

TABLE II: EXTRINSIC CALIBRATION RESULTS OF LIDARS INSIDE MID-100 IN TWO TEST SCENES

	Rotation Error (degree)		Translation Error (m)	
	mean	std	mean	std
Motion Based [13]	2.7223	2.4137	0.3955	0.1267
Proposed	**0.2173**	**0.1699**	**0.0075**	**0.0016**

2) AVIA and MID-100 LiDAR: In this section, we demonstrate that our method works well given two types of LiDARs with different FoVs and point cloud densities, and we compare the results with those from motion-based method [13]. The AVIA is chosen as the base LiDAR to calibrate the extrinsic $\mathcal{E}_L$ between AVIA and each MID-40s, i.e., ${}^{L_3}_{L_0}\mathbf{T}, {}^{L_3}_{L_1}\mathbf{T}$ and ${}^{L_3}_{L_2}\mathbf{T}$ (see Fig. 7). Then we calculate the ${}^{L_1}_{L_0}\mathbf{T}, {}^{L_1}_{L_2}\mathbf{T}$ from the above results and compare them with the known values obtained from manufacturer. For both methods, the extrinsic $\mathcal{E}_L$ are initialized by Hand-eye calibration, and the results from both test scenes are summarized in Table III. It is shown that the proposed method's performance is less affected by the distinct characteristics introduced from different types of LiDARs.

TABLE III: EXTRINSIC CALIBRATION RESULTS BETWEEN AVIA AND MID-100 IN TWO TEST SCENES

	Rotation Error (degree)		Translation Error (m)	
	mean	std	mean	std
Motion Based [13]	5.0876	4.3721	0.9945	0.5701
Proposed	**0.2510**	**0.2184**	**0.0084**	**0.0023**

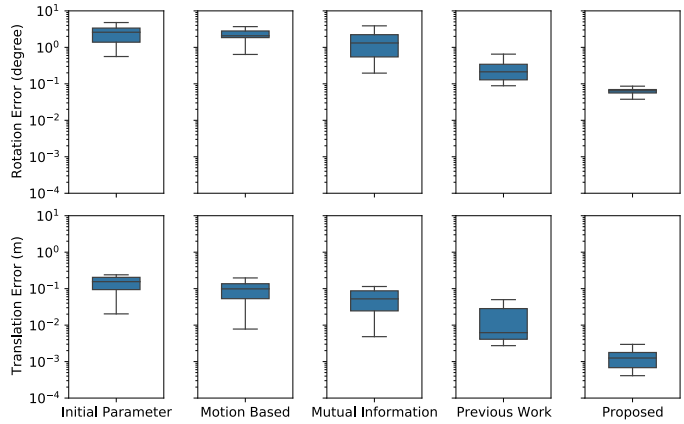

Fig. 13: Extrinsic calibration results of [9, 11, 13] and our proposed method. Each box-plot illustrates the results of 20 trials using the data collected in scene-2. The mean and standard deviation of the initial rotation error are 2.5676 and 1.3777 degrees. The mean and standard deviation of the initial translation error are 0.1460m and 0.0680m, respectively.

C. Multiple LiDAR Camera Calibration

1) Among AVIA, MID-100 and Cameras: In this section, we compare our proposed LiDAR-camera extrinsic calibration method with the motion-based [13], the mutual information based [9] methods and our previous work [11]. Both [9, 13] are targetless, utilize the intensity information of the LiDAR point cloud and match it with the edge features extracted from the image. Here, we select the AVIA as the base LiDAR and calibrate its extrinsic with respect to the three MID-40 LiDARs and the two cameras (see Fig. 7). The initial extrinsic $\mathcal{E}_C$ are calculated by adding disturbance to the values measured from the CAD model. We perform 20 independent trials with the data collected in scene-2, that in each trial the initial extrinsic is randomly perturbed ($\pm$5 degrees for ${}^{C_k}_{L_3}\mathbf{R}$ and $\pm$0.1m for ${}^{C_k}_{L_3}\mathbf{t}$) from the CAD model's measurements. We calibrate the extrinsic of each camera individually (i.e., ${}^{C_1}_{L_3}\mathbf{T}$ and ${}^{C_2}_{L_3}\mathbf{T}$), then we calculate the ${}^{C_1}_{C_2}\mathbf{T}$ and compare it with that directly calibrated by the standard chessboard method serving the ground-truth. The calibration results are illustrated in Fig. 12 and Fig. 13 and the averaged computation time is summarized in Table IV. It is seen both [9, 13] are very time-consuming as in each iteration,

TABLE IV: COMPUTATION TIME COMPARISON

	LiDAR Feature Extraction	Extrinsic Optimize Per Iteration
Motion Based [13]	-	10.7596s
Mutual Information Based [9]	-	4.8132s
Previous Work [11]	37.3052s	1.4499s
Proposed	**6.3994s**	**0.8374**

and they need to search the entire point cloud for feature correspondence matching. Moreover, the edge feature deducted from intensity information is less reliable than that calculated from plane intersections. Compared with [11], the proposed work implements the adaptive voxelization, which further improves the efficiency and accuracy. It is shown that our proposed method outperforms [9, 11, 13] both quantitatively and qualitatively.

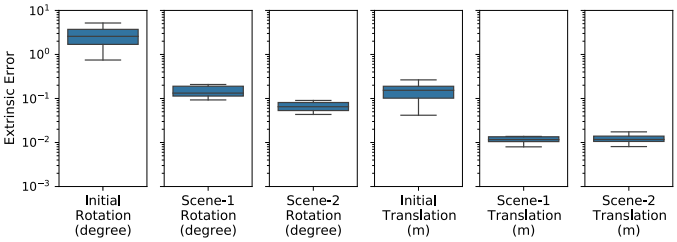

Fig. 14: Extrinsic calibration results of MID-100 and opposite pointing cameras in two test scenes. Each box-plot illustrates the results of 20 trials. The mean and standard deviation of the initial rotation error are 2.5576 and 1.2590 degrees. The mean and standard deviation of the initial translation error are 0.1417m and 0.0602m, respectively.

2) MID-100 and Cameras: In this section, we demonstrate that the proposed method could also calibrate the extrinsic $\mathcal{E}_C$ between LiDAR and cameras without FoV overlap. We choose the middle MID-40 of the MID-100 as the base LiDAR and calibrate the extrinsic of each LiDAR-camera pairs (i.e., ${}^{C_1}_{L_1}\mathbf{T}$, ${}^{C_2}_{L_1}\mathbf{T}$, see Fig. 7). The initial extrinsic $\mathcal{E}_C$ are calculated by adding disturbance to the values measured from the CAD model. We perform 20 independent trials with the data collected in both scenes, that in each trial we randomly perturb the initial extrinsic value ($\pm$5 degrees for ${}^{C_k}_{L_1}\mathbf{R}$ and $\pm$0.1m for ${}^{C_k}_{L_1}\mathbf{t}$) from the CAD's measurements. Then we calculate the ${}^{C_1}_{C_2}\mathbf{T}$ and compare it with that obtained by the standard chessboard method. The calibration results and the corresponding colorized point cloud are illustrated in Fig. 14 and Fig. 15.

It is seen that the general extrinsic calibration performance between MID-40 and cameras is less competitive than that between AVIA and cameras. This might be due to the reason that AVIA has larger FoV coverage (70.4 versus 38.4 degrees) and thus point cloud density (6 laser beams versus 1 laser beam) than MID-40, which will provide more edge correspondences in all directions. The performance of MID-40 and cameras extrinsic calibration in scene-2 is also slightly better than scene-1. This is probably due to the reason that the extracted LiDAR edges mismatch with and are trapped into the image edges largely existed on the ground of scene-1.

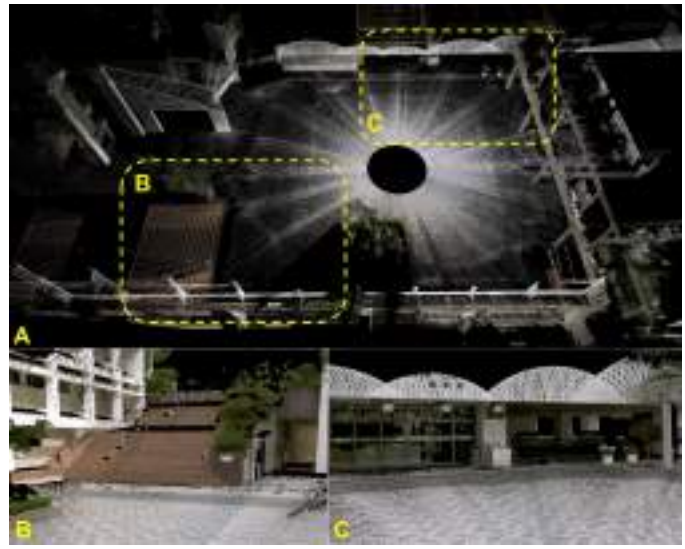

Fig. 15: Colorized point cloud of MID-100 LiDAR and the opposite pointing camera in scene-1. The left camera's images are used to color the point cloud. The brightness of the building wall is due to the reflection of the sunlight. A) Bird-eye's view. B) Details of the stairs, fence and ground tiles. C) Entrance of the library. The details of flowerpots are clearly shown.

V. Conclusion

In this paper, we propose a fast, accurate, and targetless extrinsic calibration method for multiple LiDARs and cameras. We analytically derive the derivatives of the cost function w.r.t. the extrinsic parameter and implement adaptive voxelization, which has significantly shortened the total calibration time. Experiment results under multiple LiDAR-camera configurations in outdoor test scenes demonstrate the robustness and reliability of our proposed method. Even when no FoV overlap exists between sensor pairs, our proposed method could still achieve sufficient high accuracy.

Acknowledgment

The authors thank Livox Technology and AgileX Robotics for their product support.

References

[1] F. Kong, W. Xu, Y. Cai, and F. Zhang. Avoiding dynamic small obstacles with onboard sensing and computation on aerial robots. *IEEE Robotics and Automation Letters*, 6(4):7869–7876, 2021.

[2] J. Lin and F. Zhang. Loam-livox: A fast, robust, high-precision lidar odometry and mapping package for lidars of small fov. In *Proc. of The International Conference in Robotics and Automation (ICRA)*, 2020.

[3] Z. Liu and F. Zhang. Balm: Bundle adjustment for lidar mapping. *IEEE Robotics and Automation Letters*, 6(2):3184–3191, 2021.

[4] X. Liu and F. Zhang. Extrinsic calibration of multiple lidars of small fov in targetless environments. *IEEE Robotics and Automation Letters*, 6(2):2036–2043, 2021.

[5] J. Lin, X. Liu, and F. Zhang. A decentralized framework for simultaneous calibration, localization and mapping with multiple lidars. In *2020 IEEE/RSJ International Conference on Intelligent Robots and Systems (IROS)*, pages 4870–4877, 2020.

[6] C. Gao and J. R. Spletzer. On-line calibration of multiple lidars on a mobile vehicle platform. In *2010 IEEE International Conference on Robotics and Automation*, pages 279–284, 2010.

[7] B. Xue, J. Jiao, Y. Zhu, L. Zhen, D. Han, M. Liu, and R. Fan. Automatic calibration of dual-lidars using two poles stickered with retro-reflective tape. In *2019 IEEE International Conference on Imaging Systems and Techniques (IST)*, pages 1–6, 2019.

[8] J. Levinson and S. Thrun. Automatic online calibration of cameras and lasers. In *Robotics: Science and Systems*, volume 2, page 7. Citeseer, 2013.

[9] G. Pandey, J. R. McBride, S. Savarese, and R. Eustice. Automatic extrinsic calibration of vision and lidar by maximizing mutual information. *J. Field Robotics*, 32:696–722, 2015.

[10] J. Jiao, H. Ye, Y. Zhu, and M. Liu. Robust odometry and mapping for multi-lidar systems with online extrinsic calibration. *IEEE Transactions on Robotics*, pages 1–10, 2021.

[11] C. Yuan, X. Liu, X. Hong, and F. Zhang. Pixel-level extrinsic self calibration of high resolution lidar and camera in targetless environments. *IEEE Robotics and Automation Letters*, 6(4):7517–7524, 2021.

[12] L. Heng. Automatic targetless extrinsic calibration of multiple 3d lidars and radars. In *2020 IEEE/RSJ International Conference on Intelligent Robots and Systems (IROS)*, pages 10669–10675, 2020.

[13] Z. Taylor and J. Nieto. Motion-based calibration of multimodal sensor extrinsics and timing offset estimation. *IEEE Transactions on Robotics*, 32(5):1215–1229, 2016.

[14] H. Radu and D. Fadi. Hand-eye calibration. *The International Journal of Robotics Research*, 14(3):195–210, June 1995.

[15] J. Levinson and S. Thrun. Unsupervised calibration for multi-beam lasers. *Experimental Robotics Springer Tracts in Advanced Robotics*, 79:179–193, 2014.

[16] W. Maddern, A. Harrison, and P. Newman. Lost in translation (and rotation): Rapid extrinsic calibration for 2d and 3d lidars. In *2012 IEEE International Conference on Robotics and Automation*, pages 3096–3102, 2012.

[17] M. Billah and J. A. Farrell. Calibration of multi-lidar systems: Application to bucket wheel reclaimers. *IEEE Transactions on Control Systems Technology*, page 1–12, 2019.

[18] L. Zhou, D. Koppel, and M. Kaess. Lidar slam with plane adjustment for indoor environment. *IEEE Robotics and Automation Letters*, 6(4):7073–7080, 2021.

[19] P. Geneva, K. Eckenhoff, Y. Yang, and G. Huang. Lips: Lidar-inertial 3d plane slam. In *2018 IEEE/RSJ International Conference on Intelligent Robots and Systems (IROS)*, pages 123–130, 2018.

[20] J. Kummerle and T. Kuhner. Unified intrinsic and extrinsic camera and lidar calibration under uncertainties. *2020 IEEE International Conference on Robotics and Automation (ICRA)*, 2020.

[21] Sergio A. Rodriguez F., Vincent Fremont, and Philippe Bonnifait. Extrinsic calibration between a multi-layer lidar and a camera. In *2008 IEEE International Conference on Multisensor Fusion and Integration for Intelligent Systems*, pages 214–219, 2008.

[22] Y. Park, S. Yun, C. Won, K. Cho, K. Um, and S. Sim. Calibration between color camera and 3d lidar instruments with a polygonal planar board. *Sensors*, 14(3):5333–5353, 2014.

[23] G. Koo, J. Kang, B. Jang, and N. Doh. Analytic plane covariances construction for precise planarity-based extrinsic calibration of camera and lidar. *2020 IEEE International Conference on Robotics and Automation (ICRA)*, 2020.

[24] L. Zhou, Z. Li, and M. Kaess. Automatic extrinsic calibration of a camera and a 3d lidar using line and plane correspondences. *2018 IEEE/RSJ International Conference on Intelligent Robots and Systems (IROS)*, 2018.

[25] J. Jeong, Y. Cho, and A. Kim. The road is enough! extrinsic calibration of non-overlapping stereo camera and lidar using road information. *IEEE Robotics and Automation Letters*, 4(3):2831–2838, 2019.

[26] B. Nagy, L. Kovács, and C. Benedek. Online targetless end-to-end camera-lidar self-calibration. In *2019 16th International Conference on Machine Vision Applications (MVA)*, pages 1–6, 2019.

[27] C. Park, P. Moghadam, S. Kim, S. Sridharan, and C. Fookes. Spatiotemporal camera-lidar calibration: A targetless and structureless approach. *IEEE Robotics and Automation Letters*, 5(2):1556–1563, 2020.

[28] Y. Zhu, C. Zheng, C. Yuan, X. Huang, and X. Hong. Camvox: A low-cost and accurate lidar-assisted visual slam system. *arXiv preprint arXiv:2011.11357*, 2020.

[29] D. Scaramuzza, A. Harati, and R. Siegwart. Extrinsic self calibration of a camera and a 3d laser range finder from natural scenes. In *2007 IEEE/RSJ International Conference on Intelligent Robots and Systems*, pages 4164–4169. IEEE, 2007.

[30] C. Hertzberg, R. Wagner, U. Frese, and L. Schröder. Integrating generic sensor fusion algorithms with sound state representations through encapsulation of manifolds. *Information Fusion*, 14(1):57–77, 2013.